First Light And Reionisation Epoch Simulations (FLARES) II: The Photometric Properties of High-Redshift Galaxies

Sweet, F. A.,[1]⋆ A. N. Other,[2] Third Author[2,3] and Fourth Author[3]

[1]*Astronomy Centre, University of Sussex, Falmer, Brighton BN1 9QH, UK*
[2]*Department, Institution, Street Address, City Postal Code, Country*
[3]*Another Department, Different Institution, Street Address, City Postal Code, Country*

ABSTRACT
We present the photometric properties of galaxies in the First Light and Reionisation Epoch Simulations (Flares , see Lovell et al. 2020). The intrinsic UV luminosity function provides an excellent match to observation of faint ($M_{\mathrm{FUV}} > -20$) galaxies at $z = 5 - 9$. The number of intrinsically bright galaxies predicted by Flares is significantly larger than that observed, however this can be explained through a simple model which links dust-attenuation to the metal content of the interstellar medium. In addition to predicting a range of other photometric properties we make available a public catalogue of XXXXX galaxies including their physical and photometric properties.

Key words: keyword1 – keyword2 – keyword3

1 INTRODUCTION

The past few decades have seen tremendous growth in the understanding of galaxy formation and evolution in the first billion years of the Universe after the Big Bang. The first stars and galaxies formed within the first few million years after the big bang. They were the first sources of ionising photons in the Universe, ushering in the Epoch of Reionisation (EoR) by ionising hydrogen (e.g. Wilkins et al. 2011; Bouwens et al. 2012; Robertson et al. 2013, 2015; Bouwens et al. 2015b). This period has been observable due to the efforts of the *Hubble Space Telescope* (give few citations), which have discovered numerous galaxies at high redshift by the use of dropout techniques, for $z > 5$. These efforts have also been complimented by ground based telescopes like ALMA (give few citations) and VLT (give few citations) by the spectroscopic detection of line emission from these galaxies.

With upcoming facilities like *James Webb Space Telescope* (*JWST*) and *Euclid* that can comprehensively study galaxies in the EoR, it is timely to model and predict the properties of these high redshift systems. *JWST* with better sensitivity in the IR and spatial resolution while *Euclid* can do deep and wide surveys. They can thus provide effective constraints on the bright and rare galaxies in the early Universe. This would further be the test beds for our understanding of the theory of galaxy formation and evolution giving insights into the physical processes that shape the star formation history, morphology and the impact of environment on the first galaxies.

One of the quantities in the EoR where we have extensive observational constraints is the galaxy luminosity function, measuring the comoving number density of galaxies as a function of their luminosity across different redshifts. There have been numberous studies done to quantify this value and provide insight into the this population (e.g. Bouwens et al. 2015a; McLeod et al. 2015; Finkelstein et al. 2015; Bouwens et al. 2016; Livermore et al. 2017; Atek et al. 2018; Bowler et al. 2019).

Another exciting area which is currently being probed are line luminosities and their equiwalent widths. Lyman alpha has been primarily used for spectroscopic confirmation of high-redshift galaxies, but they become increasingly weak at higher-redshift due to increasing neutral fraction in the inter-galactic medium (IGM). Rest-frame far infrared lines are also useful probe of galaxies in the EoR. ALMA has found mixed success in detecting the brightest of the far-infrared line [CII] and in descovering [OIII] lines even in one of the highest redshift galaxies (citations). With many of the emission lines in the optical arising from HII regions rather than from PDRs, it also makes their modelling easier. With most of the current existing constraints in the EoR being mostly luminosity functions in the UV; this is going to change with the lauch of *JWST* whose onboard instruments will provide access to many of the strong emission lines in the EoR.

Complementary to this many theoretical works on simulations of galaxy evolution have been used to study the population of galaxies and their properties in the EoR. For testing the validity of these theoretical models, they need to make predictions on the various observables. There are various intrinsic physical properties of galaxies like stellar mass, star formation rate, that are available directly from simulations which can be compared to that of observed galaxies. These all involve some modelling assumptions based on the star formation history or metallicity of the observed galaxies, which are hard to derive with limited available data on the galaxy at these high

---

⋆ E-mail: mn@ras.org.uk (KTS)

redshifts. Another approach is to make predictions from simulations to compare that to galaxy observables that suffer from comparatively less modelling biases and thus giving us more insights into the physical processes that takes place in these galaxies.

Semi-Anlytical Models, which run on halo merger trees extracted from dark matter only simulations or Extended Press-Schechter methods have been widely used and very successful in the study of galaxy formation and evolution. A number of these studies (citations) have been used to make predictions on the observables in the EoR. They are powerful tools that can be applied to large cosmological volumes to extend the range of the probed distribution functions or observables due to their shorter computation times, but they rely on analytical recipes thus do not self-consistently evolve various interactions, hence requiring additional steps and approximations to retrieve observables.

Hydrodynamical simulations of galaxy formation that self-consistently trace the evolution of dark matter, gas, stars and black holes are another tool to study the evolution of galaxy properties. Many state of the art periodic cosmological volumes (citations) have been undertaken and they have been successful in reproducing many of the observables, but only few of these simulation suites have the capability to provide the large scale power to replicate these observations. Even then the enormous computational time to run these large periodic boxes have prevented us from exploring large dynamic ranges with better resolution. There have been high resolution zoom simulations that have probed the EoR (citations) but not necessarily extended the dynamic range that will be probed by the next generation surveys. For the purpose of studying this epoch in the Universe, we have run a suite of zoom-in simulations probing a range of overdensities, termed Flares; see Lovell et al. (2020), hereafter PaperI.

In this article we use the Flares suite of resimulations to predict the photometric properties of the galaxies in the FLARE which will be accessible to the upcoming Webb, Euclid, WFIRST, telescopes, thus providing insights into current galaxy modelling physics of the high redhisft Universe. We begin by briefly introducing the simulation suite in Section 2 and our modelling of galaxy observables in Section 2.2 and 2.3. In Section **??** we focus on the derived photometric properties of the simulated galaxies and present our conclusions in Section 5. We assume a Planck year 1 cosmology (Ω_m = 0.307, Ω_Λ = 0.693, h = 0.6777; Planck Collaboration et al. 2014).

2   FIRST LIGHT AND REIONISATION EPOCH SIMULATIONS

Flares is a suite of zoom simulations targeting a range of overdensities in the Epoch of Reionisation (EoR). The regions are drawn from the same 3.2Gpc a side dark matter only, parent simulation box used in the C-Eagle simulations Barnes et al. (2017). The selection of regions is done at z = 4.67, the highest redshift snapshot available for this simulation, from which we select 40 spherical regions with a radius of 14h^{-1}Mpc spanning a wide range of overdensities. This redshift selection also ensures that the extreme overdensities are mildly non-linear, and thus more or less preserves the rank ordering of overdensities at higher redshifts. We have deliberately selected more number of extreme overdensity regions to obtain a large sample of the first massive galaxies that form in the Universe. We also select a number of regions with intermediate and mean overdensities as well as a few underdense regions to better sample the density space and explore the impact of environment on galaxy

formation. These regions are then re-simulated with full hydrodynamics using the AGNdT9 configuration of the Eagle simulation physics as described in Schaye et al. (2015); Crain et al. (2015). The regions are combined using appropriate weightings to obtain a representative sample of the Universe. For a full description of the simulation and weighting method we refer the readers to PaperI.

2.1   Galaxy Identification

Galaxies in Flares similar to the standard Eagle analysis are identified with Subfind (citation) algorithm within bound groups found from the Friends-Of-Friends (FOF, citation) algorithm. The stellar masses are defined using star particles within a 30pkpc aperture centred around the most bound particle of the substructure. In this work we concentrate on a more limited definition of a galaxy focusing on only those objects with a combined total of more than 100 gas and star particles. This extends the stellar mass function to ~ $10^{7.5}$M$_\odot$ at z = 5.

Flares have more than ~20 times the number of galaxies greater than 10^{10} M$_\odot$ at z = 5 compared to the Eagle reference volume (Schaye et al. 2015) in the combined volume we resimulate (see Figure 5 in PaperI). In Figure 1 we compare the galaxy stellar mass function of the galaxies in Flares , the Eagle simulations and the BlueTides volume. It can be seen that Flares extend the range by atleast an order of magnitude at the high mass end compared to Eagle , and by ~0.5 dex with respect to BlueTides (Feng et al. 2015). We explore the results, presenting the various galaxy observables in the coming sections.

2.2   Spectral Energy Distribution Modelling

2.2.1   Stellar Emission

We begin by modelling the pure stellar emission produced by each galaxy. To do this we associate each star particle with a stellar SED according to its age and metallicity (i.e. a simple stellar population or SSP). We assume a Chabrier IMF throughout (Chabrier 2003).

2.2.2   Nebular Emission

... they produce significant Lyman-continuum (LyC). To account for the reprocessing of these photons by surrounding gas we associate each star particle with a surrounding H$_{II}$ region powered by its LyC emission. To calculate the nebular emission we follow the approach detailed in XXX and use the cloudy (ref) photo-ionisation modelling code. Specifically we assume ...

2.3   Dust Attenuation

To compare to the galaxy observables at this redshift requires treatment of the simulation data to create mock observations. One of the most important ingredient in generating such mock observations involves modelling the attenuation by dust. It has a major impact on the observed properties of galaxies with almost 30% of all photons in the Universe having been reprocessed by dust grains at some point in their lifetime. There have been a few studies that have incorporated dust creation and destruction self-consistently into hydrodynamical simulations (citations), but these are compuationally intensive and involve additional subgrid recipes which are poorly understood. A simple alternative is to model the effect of dust based on the properties of stars and gas particles in the simulation.

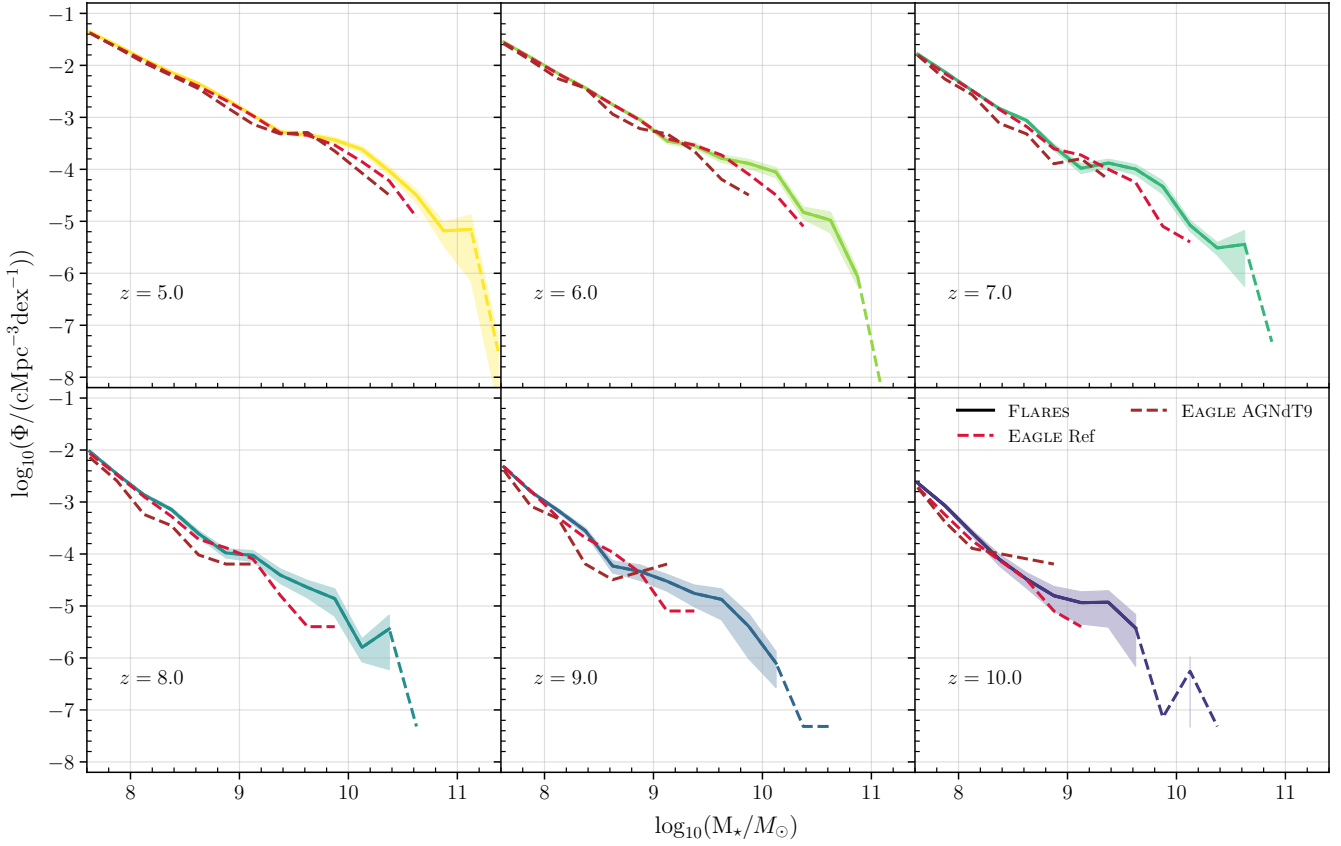In this work, for estimating the attenuation by dust, each star

Figure 1. FLARES composite galaxy stellar mass function (black solid, dashed for bins with less than 3 galaxies) for z ∈ [5,10]. Shaded region denote the poisson 1σ uncertainties for each bin from the simulated number counts for the FLARES dust attenuated UV LF. For comparison the GSMF from the EAGLE Reference, EAGLE AGNdT9 and BlueTides simulation boxes.

particle treated is as a point in space with it's emitted light reaching the observer through the intervening gas particles, with the viewing angle fixed to be along the z-axis. The effect of any star particle along the same line-of-sight (LOS) is ignored. For the purpose of this study we link the metal column density ($\Sigma(x, y)$) integrated along the LOS (z-axis) to the dust optical depth in the V-band (550nm) due to the intervening interstellar medium (ISM) $\tau_{\mathrm{ISM,V}}(x, y)$, the same approach as in Wilkins et al. (2017). This relation can be expressed as

$$\tau_{\mathrm{ISM,V}}(x, y) = \kappa_{\mathrm{ISM}}\Sigma(x, y) \tag{1}$$

where κ_{ISM} is a normalization parameter which we have chosen to match the rest-frame far-UV (1500Å) luminosity function to the observed UV luminosity function from Bouwens et al. (2015a) at $z = 5$. Thus κ_{ISM} acts as a proxy for the properties of dust such as the average grain size, shape, composition as well as the dust-to-metal ratio in the ISM. It is worthwhile to note that dust-to-metal ratios of galaxies not necessarily be constant across redshift, but possibly a function of their evolutionary stage (see De Vis, P. et al. 2019; Vijayan et al. 2019, etc) with the median value decreasing with increasing redshift. Hence this may cause our simple model to overpredict the attenuation of galaxies progressively with redshift. In a companion work we explore the impact of a range of different modelling approaches. $\Sigma(x, y)$ is obtained by integrating the density field of particles along the z-axis with the smoothing kernel of the SPH particle. FLARES uses the same flavour of SPH used by EAGLE,
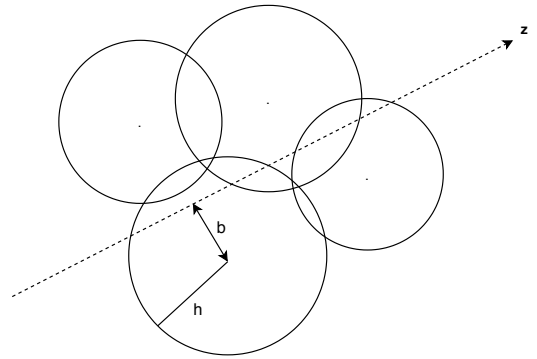

Figure 2. Line of sight tracing of the sph density field, with the circles representative of sph particles. h and b denote the smoothing length of the corresponding gas particle and the impact parameter to the line of sight ray respectively.

termed SPH-ANARCHY (see Schaller et al. 2015, for more details). The kernel function can be expressed as follows:

$$W(r, h) = \frac{21}{2\pi h^3} \begin{cases} (1 - \frac{r}{h})^4(1 + 4\frac{r}{h}) & \text{if } 0 \le r \le h \\ 0 & \text{if } r > h \end{cases} \tag{2}$$

where h is the smoothing length of the corresponding particle and r is the distance from the centre of the particle. The smoothed density line integral across a particular particle can be calculated by using

the impact parameter, b which is calculated from the centre of the particle (illustrated in Figure 2). Using the impact parameter of every gas particle in front of the selected stellar particle, the LOS metal column density can be calculated as follows:

$$\Sigma(x, y) = 2 \sum_i Z_i m_i \int_0^{\sqrt{h_i^2 - b_i^2}} W(r, h_i) dz \, ; \, r^2 = b_i^2 + z^2 \quad (3)$$

where the index 'i' denote gas particles along the LOS, with Z and m the metallicity and mass of the particle respectively. To simplify this calculation, impact parameters can be normalized with the smoothing length, and thus generate pre-computed values of the LOS metal density which can be readily used to compute the density for arbitrary values of smoothing length and impact parameters.

Other than the dust extinction along the LOS, there is an additional component of dust that affects young stellar populations that are still embedded in their birth cloud. Effect of the birth cloud attenuation in our galaxies is a phenomenon that happens below the resolution scale, since stellar clusters form on sub-kpc scales. The birth cloud dust optical depth in the V-band for our model can be expressed in a similar manner to equation.1 as

$$\tau_{BC,V}(x, y) = \begin{cases} \kappa_{BC}(Z/0.01) & t \leq 10^7 \text{yr} \\ 0 & t > 10^7 \text{yr} \end{cases} \quad (4)$$

where κ_{BC} just like κ_{ISM}, is a normalization factor, while Z is the metallicity of the stellar particle with age less than 10^7yr, following the assumption from Charlot & Fall (2000) that birth clouds disperse on these timescales. Hence only those young stellar particles are affected by this additional attenuation. With these parameters the optical depth in the V-band is linked to other wavelength using a simple simple power-law relation

$$\tau_\lambda = (\tau_{ISM} + \tau_{BC}) \times (\lambda/550\text{nm})^{-1} \quad (5)$$

As discussed earlier there are two free parameters in our model, κ_{ISM} that links the optical depth in the ISM to the LOS metal surface density and κ_{BC} linking the stellar particle metallicity to the optical depth due to the presence of a birth cloud in young stellar populations. The value for these parameters in our model is obtained by first varying κ_{BC} within a range of (0.0001, 3.) to get a value for κ_{ISM} by fitting the observed UV luminosity function from Bouwens et al. (2015a) at $z = 5$. We choose κ_{BC} so as to match observations of the UV-continuum slope (β) as well as the equivalent-width (EW) relations (OIII doublet and H$_\beta$) from De Barros et al. (2019), while κ_{ISM} follows naturally from this. We would also like to point out that our selection of κ_{BC} is a way to incorporate both of these observations, as a higher value is favoured to get better agreement with the UV-continuum observations while the EW relations prefer a lower value. The reasoning behind our choice of both κ_{ISM} and κ_{BC} as well as the parameter search is explained further in Appendix A. This study uses $\kappa_{BC} = 1.25$ and $\kappa_{ISM} = 0.0063$ for all the redshifts considered in this study. We would like to remind the reader that this implies no evolution in the dust-to-metal ratio as well as the general properies of the dust grain in galaxies.

We show in Appendix C how some of the observables presented in the next sections change on using different extinction curves available from literature.

3 UV LUMINOSITY FUNCTION

The UV LF evolution of high redshift galaxies is a regime where there are numerous observational studies done. We begin by calcu-

lating the rest-frame ultraviolet (UV) luminosity function (LF) of the Flares galaxies.

3.1 LF creation

Unlike the simulation of a periodic box the re-simulation strategy of Flares means that the luminosity function (or stellar mass function) is not simply straightforward. The contribution from any resim region needs to weighted by the appropriate weight for that region. The weighting strategy of Flares has been explained in detail in §2.3 in PaperI, we refer the readers there for more details. With the chosen values of $\kappa_{BC} = 1.25$ and $\kappa_{ISM} = 0.0063$ explained in §2.3, we present the obtained UV luminosity funtion of $z \in [5, 10]$.

This work as presented in §2.1, we concentrate on a more limited definition of a galaxy focusing on only those objects with a combined total of more than 100 gas and star particles, extending the stellar mass function to $\sim 10^{7.5} M_\odot$ at $z = 5$. For the luminosity function we set the low brightness cut-off for the selected galaxies to be the 97th percentile of the Magnitude computed for 100 gas and star particles, allowing us to probe down to $\sim$-17 in FUV rest-frame magnitude at $z = 5$.

3.2 Luminosity Functions

We plot the dust-attenuated (as described in §2.3) UV LF in Figure 3 (solid line) along with the intrinsic LF (dashed line). Here the plotted data for Flares are in bins of width 0.5Mags, with their 1 sigma Poisson scatter. Also plotted are the Reference and AGNdT9 configuration of the Eagle simulation suite. It can be seen clearly that the luminosity function is extended to brighter galaxies by 2 Magnitudes or more at all redshifts, thus failing to probe the bright end of the UV LF. It is evident that at the faint-end the simulations agree. The bin centre and the number density per magnitude for the Flares galaxies are provided in Appendix B as Table B1.

From Figure 3 it can be seen that the observed LF is slightly lower than the intrinsic LF at luminosities fainter than ~ -20. The reason for this is the implementation of a birth cloud component for young stellar populations. Studies of exploring the impact of birth cloud attenuation has shown that this can reduce the luminosities by ~ 0.3 dex for galaxies in the local Universe (e.g. Trayford et al. 2017). Since the surface density of metals in the faint galaxies is insufficient to produce siginficant attenuation in the ISM, the choice of birth cloud component is most pronounced in this regime. While in the case of the bright end, the main contribution is from the dust attenuation in the ISM.

It is important to take note that both these regimes can be affected by the choice of initial mass function, the SPS model (see Wilkins et al. 2016) and the attenuation law. We also do not take into account the contribution of black hole accretion to the galaxy luminosity function; this will become particularly important for the bright end, but is complicated to model (Steve could say something about this).

The observed UVLF can be described by a Schechter function (e.g. Bouwens et al. 2015a; Finkelstein et al. 2015), characterized by a power law at the faint end with slope α, with an exponential cutoff at the bright end at a characteristic magnitude M*, with the parameter ϕ^* setting the normalization of this function. The number density at a given magnitude is then given by

$$\phi(M) = 0.4 \ln 10 \, \phi^* \, 10^{-0.4(M-M^*)(\alpha+1)} \, e^{-10^{-0.4(M-M^*)}} \quad (6)$$

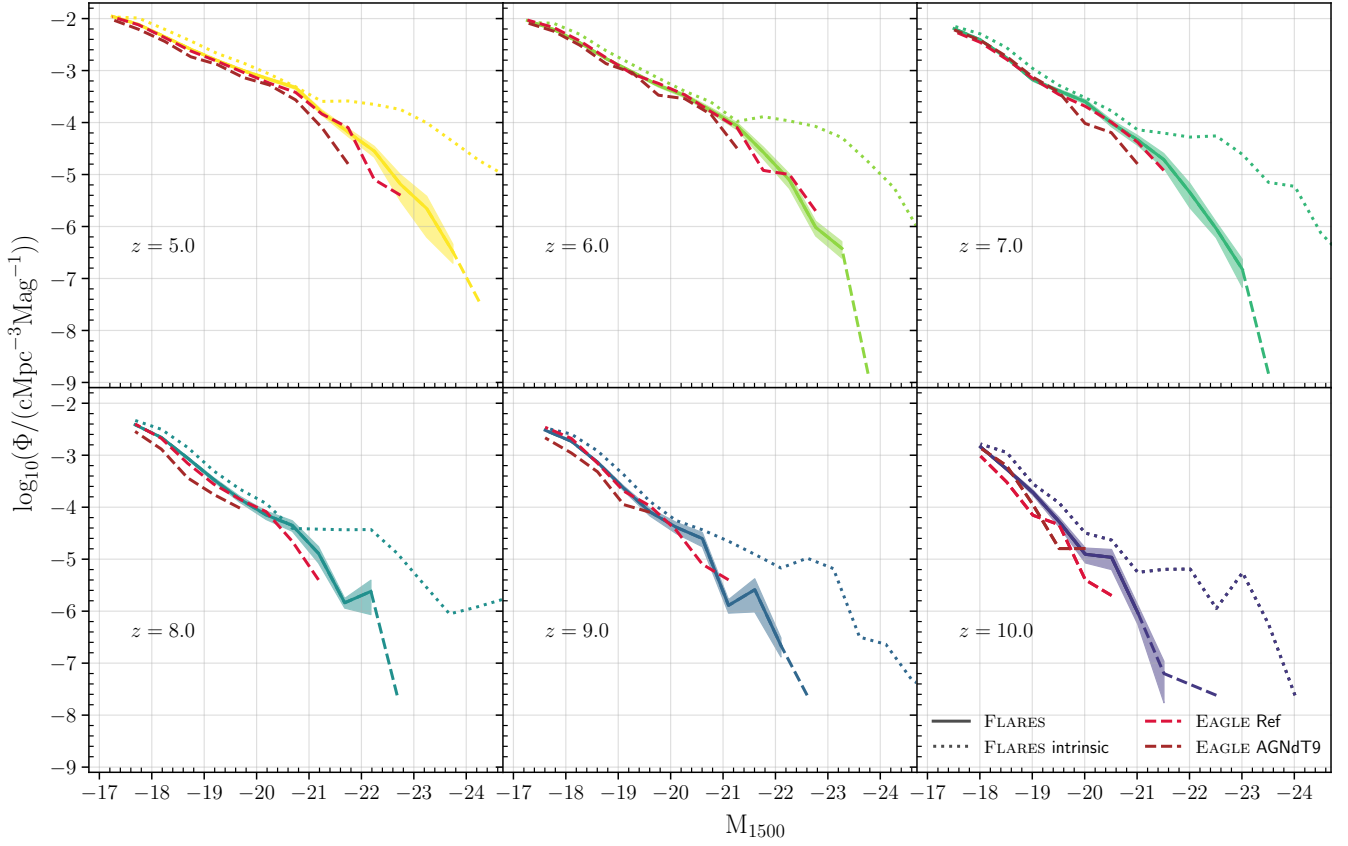To provide an easier comparison with other work we also calculate

Figure 3. FLARES composite intrinsic (dotted) and dust attenuated (solid, dashed for bins with less than 3 galaxies) UV LF for galaxies in z ∈ [5,10]. Shaded region denote the poisson 1σ uncertainties for each bin from the simulated number counts for the FLARES dust attenuated UV LF. For comparison the UV LF from the EAGLE Reference and AGNdT9 volume are plotted.
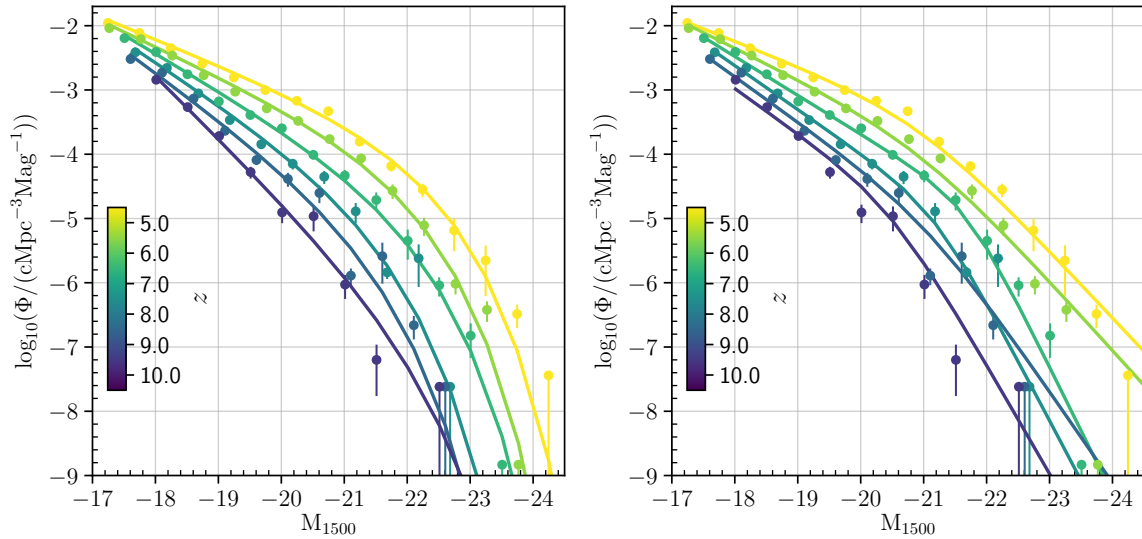

Figure 4. Schechter (left) and double power-law (right) fits to the FLARES UV LF are plotted as solid lines while the data is shown as points with the error-bars denote the 1-σ Poisson errors.
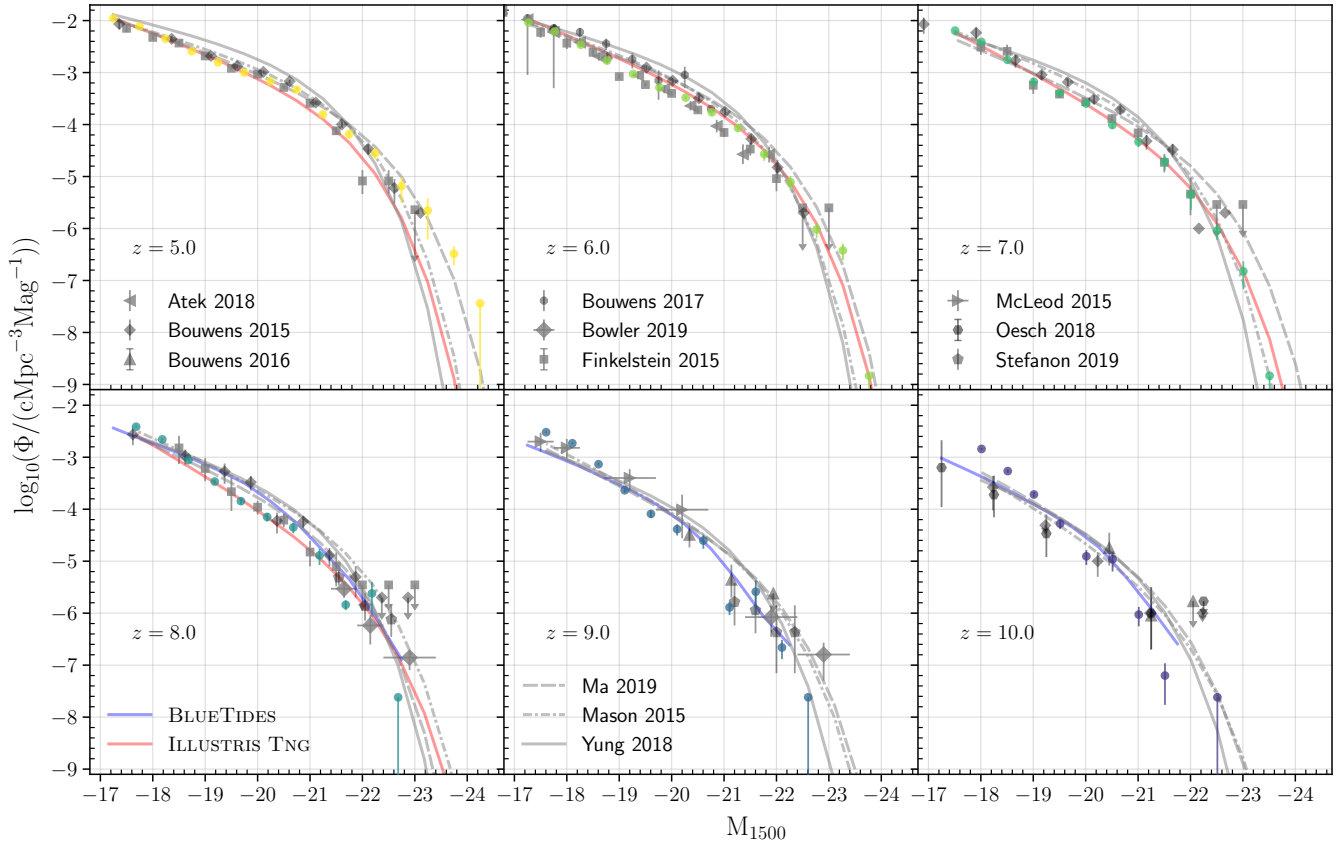
Figure 5. UV LF for Flares galaxies, with the corresponding Schechter (coloured solid) and double power-law (coloured dashed) fit is plotted for z ∈ [5,10]. Error bars denote the poisson 1σ uncertainties for each bin from the simulated number counts for the Flares dust attenuated UV LF. Observational data from Bouwens et al. (2015a); McLeod et al. (2015); Finkelstein et al. (2015); Bouwens et al. (2016, 2017); Oesch et al. (2018); Atek et al. (2018); Stefanon et al. (2019); Bowler et al. (2019) are plotted as well as the binned luminosities from BlueTides (Wilkins et al. 2017) and the Schechter fits from Ma et al. (2019); Yung et al. (2019); Illustris Tng (Model-C from Vogelsberger et al. 2020) are shown for comparison.

the Schechter function parameters of our LFs. The Schechter fits to the UV LF of Flares galaxies is shown in Figure 4 (top panel). We find that the function provides a good fit to the shape of the overall UV LF. The best-fitting schechter parameters to the UVLF are shown in Table B2. It should be noted that in case of z = 9 we set narrow priors for M*, which was done by visual inspection.

There has also been some studies that has shown a double power-law can also be used to describe the shape of the UV LF at higher redshifts (e.g. Bowler et al. 2014). The parameterization for a double power-law is as follows

$$\phi(M) = \frac{\phi^*}{10^{0.4(M-M^*)(\alpha+1)} + 10^{0.4(M-M^*)(\beta+1)}} \tag{7}$$

where α and β are the faint-end and bright-end slopes, respectively, M* is the characteristic magnitude between these two power-law regimes, and ϕ^* is the normalisation. The double power-law fit to the binned luminosities is shown in Figure 4 (bottom panel). It should be noted that we also provided narrow priors to M* at z = 9, 10 to constrain the fit. The best-fitting double power-law parameters to the UVLF are also shown in Table B2. It can be seen that this also provides a good fit to the UV LF eventhough it can overestimate the number density at the brightest end for z < 7.

We have already shown in Lovell et al. (2020) that the galaxy stellar mass function follows a double Schechter shape in Flares. It can be seen in Figure 3 that the intrinsic UV LF also has a double

Schechter shape, but the observed UV LF does not. It lies much closer to a Schechter or a double power-law shape depending on the redshift in Flares. This can be explained by dust attenuation suppressing the intrinsically bright galaxies at the knee and beyond.

We compare the performance of the two functional forms across redshifts by computing the Bayesian Information Criterion (BIC, see Schwarz 1978; Liddle 2007, and references therein for further details; also see Appendix B) for the best-fit parameters. A model with a lower BIC is preferred. For this purpose we give the difference between the BIC values of the double power-law and the Schechter best-fit values. As can be seen a Schechter function is a much better fit to the UV LF at all redshifts except at z = 7. The double power-law fit also seems to do a good job at z = 8 eventhough BIC prefers the Schechter function. Some analysis of the observational data (e.g. Bowler et al. 2014, 2019) have shown that there is not much evolution in the bright end of the galaxy luminosity function because of the lack of quenched galaxies at these redshifts, favouring a double power-law fit to the population.

3.3 Comparison with Observations and Models

The UV LF of Flares galaxies is compared to observational values from Bouwens et al. (2015a); McLeod et al. (2015); Finkelstein et al. (2015); Bouwens et al. (2016, 2017); Oesch et al. (2018); Atek et al.
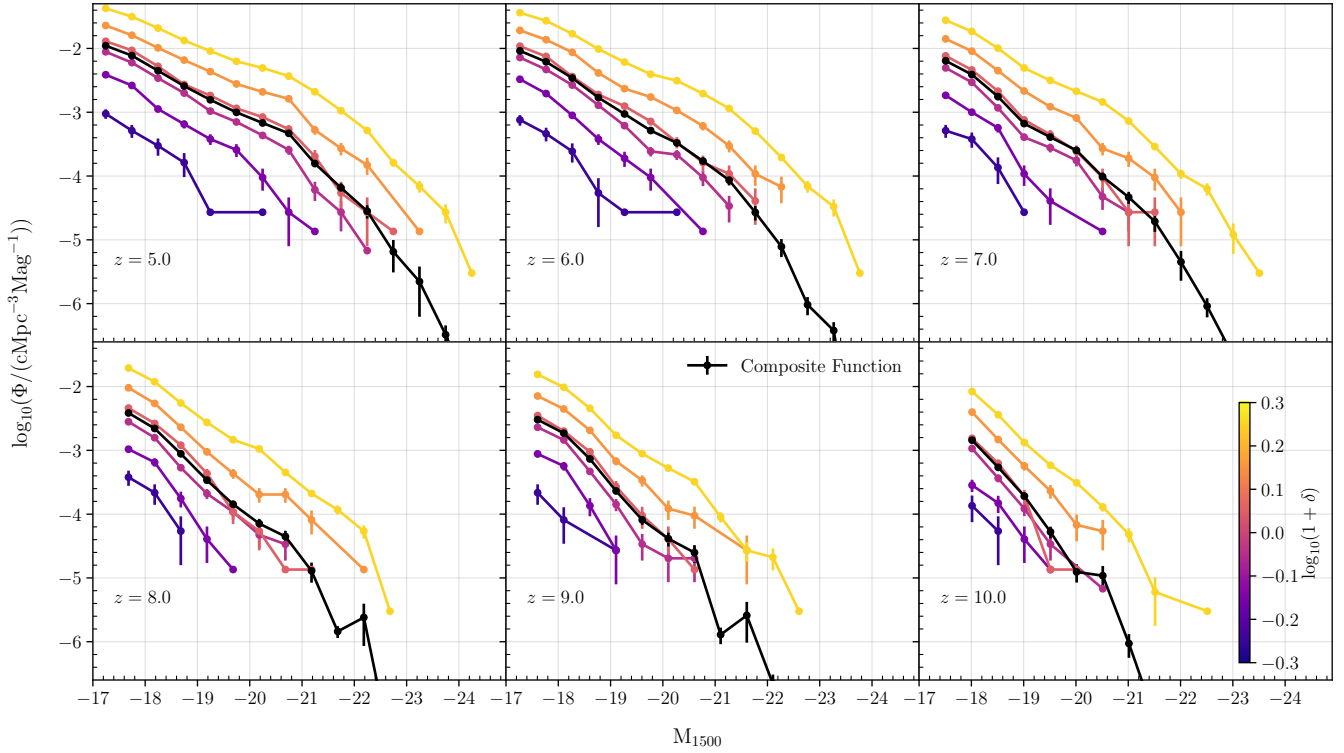
Figure 6. The FLARES UVLF for $z \in [5, 10]$ split by binned log-overdensity. Error bars denote the poisson 1σ uncertainties for each bin from the simulated number counts.
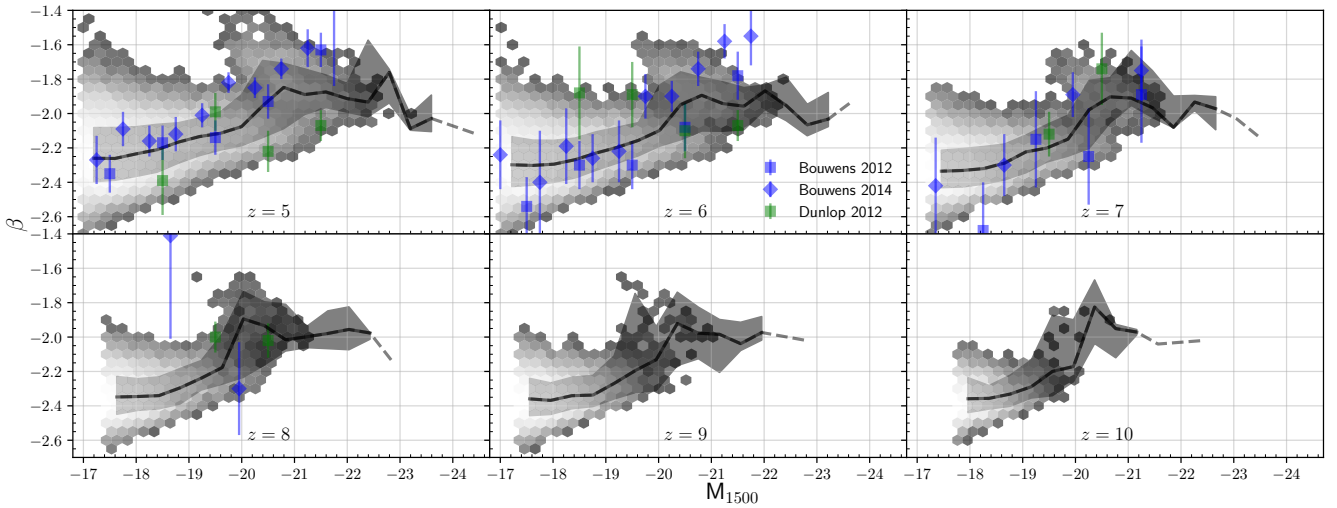

Figure 7. UV-continuum slope, β is plotted against the UV magnitude for $z \in [5, 8]$. The solid dashed line is the weighted median of the sample, with the shaded region indicating the weighted 84 and 16 percentiles. The hexbin denotes the distribution of our sample, only plotted are bins with more than 5 data points. Plotted alongside are bservational values from Dunlop et al. (2012); Bouwens et al. (2012, 2014).

(2018); Stefanon et al. (2019); Bowler et al. (2019) in Figure 5. The Schechter as well as the double power-law fit to the FLARES population is also shown.

We predict the UV LF relation at all redshift well in comparison to the observations, while slightly underpredicting the luminosities of galaxies as we progress to higher redshifts. But it should also be noted that the uncertainties in the observations gets progressively larger with increasing redshift and some of the number densities at the bright end are upper limits.

In Figure 5, we also plot the binned luminosities from BLUETIDES (Wilkins et al. 2017) and the Schechter function fits from FIRE-2 (Ma et al. 2019); SANTACRUZ SAM (Yung et al. 2019);
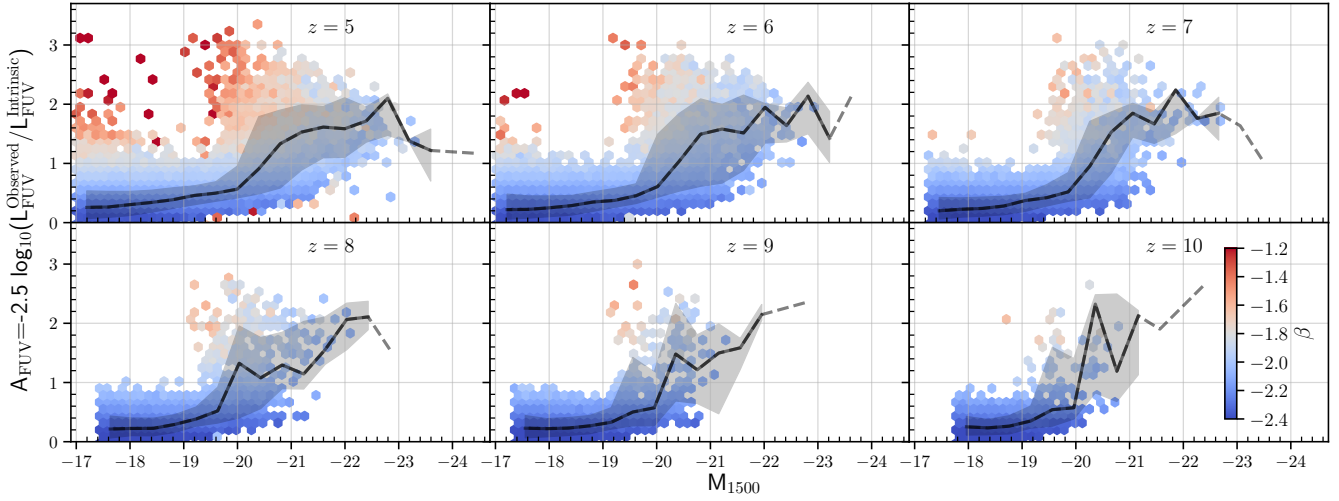
Figure 8. The attenuation in the FUV is plotted against the observed UV magnitude for $z \in [5, 10]$. The solid and dashed black line is the weighted median of the sample, with the shaded region indicating the weighted 84 and 16 percentiles. The dashed line is for bins that have less than 3 data points. The hexbin denotes the distribution of our sample, coloured by the median β value in the hexbin.
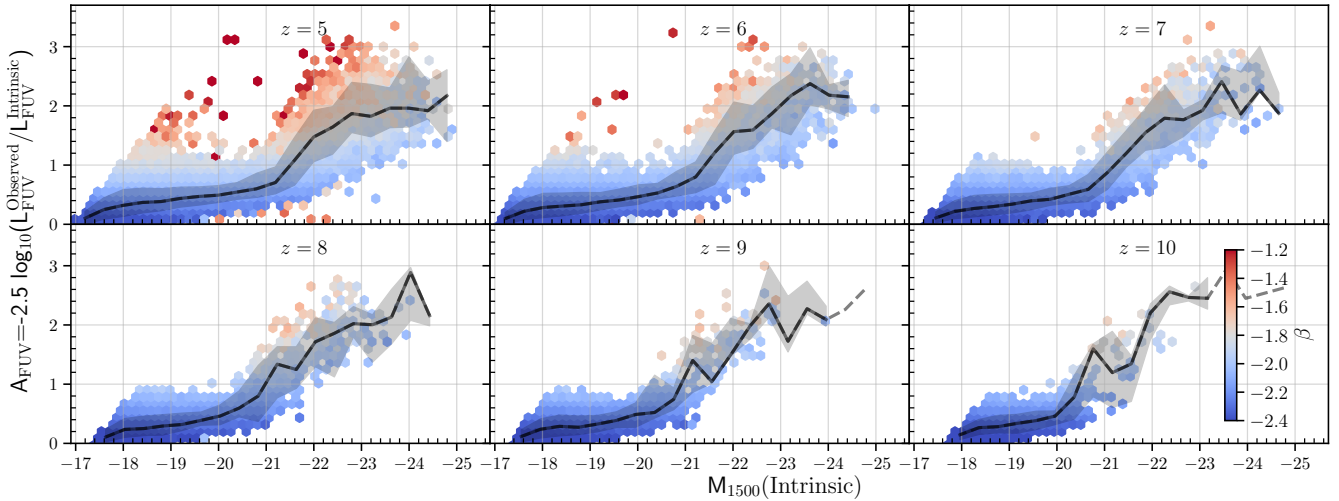

Figure 9. The attenuation in the FUV is plotted against the intrinsic UV magnitude for $z \in [5, 10]$. The solid and dashed black line is the weighted median of the sample, with the shaded region indicating the weighted 84 and 16 percentiles. The dashed line is for bins that have less than 3 data points. The hexbin denotes the distribution of our sample, coloured by the median β value in the hexbin.

ILLUSTRIS TNG (Model-C from Vogelsberger et al. 2020). As can be seen the fit is similar to others from literature, and only diverges at $z \geq 8$. This could be a consequence of the larger dynamic range probed by FLARES or the modelling differences across the studies. With respect to BLUETIDES, a comparison of data have shown us that the most massive galaxies in FLARES are more metal rich by ~0.1dex.

Also shown is the evolution of the schechter fit parameters with redshift in Figure **??**. should we include a plot about the evolution of UVLF fit parameters??

3.4   Effect of environmental on UV LF

The FLARES simulation probes galaxies that reside in a wide range of environments allowing us to analyse the effect environment has on their properties. In Figure 6 we look at how the UV LF varies as a function of overdensity for $z \in [5, 10]$. As expected the number of galaxies increases with increasing overdensity and the brighter galaxies reside in denser environments. The normalization shows a variation of ~ 2 dex from the low to the highest density environment probed in FLARES. The composite distribution function follows closely the mean density region as expected, in the regimes below the bright end, with the contribution to the bright end only coming from the densest environments.

As can be seen from Figure 6 the shape of the luminosity function is similar across various environments with the slope be-

coming steeper with decreasing density. Fit schechter functions to each of them? There is a hint of a double power-law shape in the intermediate density environments while the densest regions follow a Schechter shape. This could be due to more number of galaxies being sampled in the denser environmnets or due to different assembly histories of these galaxies driven by the environement. The effect of environment on assembly history as well as on astronomical surveys will be probed in a future work (Thomas et al. 202? in prep.).

3.5 UV continuum slope (β)

The UV continuum slope β, defined such that f$_\lambda \propto \lambda^\beta$, has been studied by different groups (citations), available due to deep near-IR observations using the Wide Field Camera 3 (WFC3) on the *Hubble Space Telescope*. This allows us to probe the rest-frame UV continuum at $z > 5$. These studies have shown that β is particularly sensitivity to the metallicity, age, and especially the dust content within a galaxy, and thus it is a useful quantity to check the reliability of theoretical models. But it is important to note that β is also strongly dependent the modelling assumption in theoretical studies like the choice of the IMF, SPS model, dust modelling and extinction law.

Figure 7 plots the value of β against the UV luminosity of the galaxies in Flares. Observational values of β from Dunlop et al. (2012); Bouwens et al. (2012, 2014) are plotted alongside for comparison. It should be noted that the observational data shows a lot of scatter and the different datasets does not show the same trends. Our weighted median of β's match observational values for almost all luminosities. At the bright end, M$_{1500} < -20$ the Bouwens et al. (2012, 2014) data predict much steeper β's compared to our results while Dunlop et al. (2012) shows lower values. This could be due to the choice of our extinction curve, a steeper/shallower curve might make for a steeper/shallower relation. The β values are an excellent constrain on the theoretical extinction curves, giving insights into the dust properties within the galaxy (see Salim & Narayanan 2020, for an overview). We try different extinction curves from literature in Appendix C.

In Figure 8 we plot the attenuation in the FUV agains the FUV luminosity, in hexbins coloured by the median β value. As can be seen from plot, most of the galaxies in Flares have lower β values even when the overall attenuation is high. This could be because there might be star particles in our simulation that reside in lines-of-sight that suffer little to no dust extinction making them bright. Another explanation is stellar migration, with stars moving out of the plane of the galaxy thus suffering less effects of dust depending on the viewing angle or geometry.

4 LINE LUMINOSITIES AND EQUIVALENT WIDTHS

- Brief introduction to what we are going to show
    - Comparison to observational and other modelling studies show [OIII] de barros data
    Halpha redshift evolution?
    line luminosity function for some lines: which ones?
    CIII]1909 and Lyman-alpha or metallicity comparison?

In this section we will present some of the nebular emission line properties and compare to some of the available observational constraints.

In Figure 10 is plotted the values of [OIII]λ4959,5007 line

luminosities as well as the equivalent widths of Flares galaxies against some of the observables.

5 CONCLUSIONS

REFERENCES

Atek H., Richard J., Kneib J.-P., Schaerer D., 2018, MNRAS, 479, 5184
Barnes D. J., Kay S. T., Henson M. A., McCarthy I. G., Schaye J., Jenkins A., 2017, MNRAS, 465, 213
Bouwens R. J., et al., 2012, ApJ, 754, 83
Bouwens R. J., et al., 2014, ApJ, 793, 115
Bouwens R. J., et al., 2015a, ApJ, 803, 34
Bouwens R. J., Illingworth G. D., Oesch P. A., Caruana J., Holwerda B., Smit R., Wilkins S., 2015b, ApJ, 811, 140
Bouwens R. J., et al., 2016, ApJ, 830, 67
Bouwens R. J., Oesch P. A., Illingworth G. D., Ellis R. S., Stefanon M., 2017, ApJ, 843, 129
Bowler R. A. A., et al., 2014, MNRAS, 440, 2810
Bowler R. A. A., Jarvis M. J., Dunlop J. S., McLure R. J., McLeod D. J., Adams N. J., Milvang-Jensen B., McCracken H. J., 2019, arXiv e-prints, p. arXiv:1911.12832
Calzetti D., Armus L., Bohlin R. C., Kinney A. L., Koornneef J., Storchi-Bergmann T., 2000, ApJ, 533, 682
Chabrier G., 2003, PASP, 115, 763
Charlot S., Fall S. M., 2000, ApJ, 539, 718
Crain R. A., et al., 2015, MNRAS, 450, 1937
De Barros S., Oesch P. A., Labbé I., Stefanon M., González V., Smit R., Bouwens R. J., Illingworth G. D., 2019, MNRAS, 489, 2355
De Vis, P. et al., 2019, A&A, 623, A5
Dunlop J. S., McLure R. J., Robertson B. E., Ellis R. S., Stark D. P., Cirasuolo M., de Ravel L., 2012, MNRAS, 420, 901
Feng Y., Di-Matteo T., Croft R. A., Bird S., Battaglia N., Wilkins S., 2015, arXiv:1504.06619 [astro-ph]
Finkelstein S. L., et al., 2015, ApJ, 810, 71
Foreman-Mackey D., Hogg D. W., Lang D., Goodman J., 2013, PASP, 125, 306
Liddle A. R., 2007, MNRAS, 377, L74
Livermore R. C., Finkelstein S. L., Lotz J. M., 2017, ApJ, 835, 113
Lovell C. C., Vijayan A. P., Thomas P. A., Wilkins S. M., Barnes D. J., Irodotou D., Roper W., 2020, arXiv e-prints, p. arXiv:2004.07283
Ma X., et al., 2019, arXiv e-prints, 1902, arXiv:1902.10152
McLeod D. J., McLure R. J., Dunlop J. S., Robertson B. E., Ellis R. S., Targett T. A., 2015, MNRAS, 450, 3032
Narayanan D., Conroy C., Davé R., Johnson B. D., Popping G., 2018, ApJ, 869, 70
Oesch P. A., Bouwens R. J., Illingworth G. D., Labbé I., Stefanon M., 2018, ApJ, 855, 105
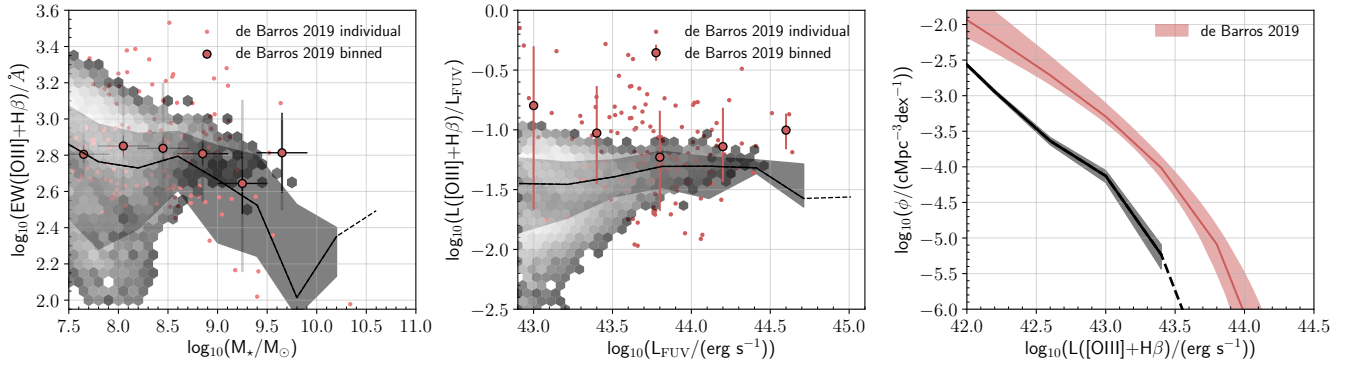Pei Y. C., 1992, ApJ, 395, 130
Planck Collaboration et al., 2014, A&A, 571, A1

Figure 10. Left: Predicted distribution of combined Hβ and [OIII]λ4959,5007 equivalent widths and stellar masses for Flares galaxies at $z \sim 8$. Middle: Predicted distribution of the Hβ and [OIII]λ4959,5007 line luminosities to the far-UV luminosity and far-UV luminosities of Flares galaxies at $z \sim 8$. In both the left and middle panel the solid dashed line is the weighted median of the sample, with the shaded region indicating the weighted 84 and 16 percentiles. The hexbin denotes the distribution of our sample, only plotted are bins with more than 5 data points. The small red circles show the individual measurements from De Barros et al. (2019) while the large points denote the median value in bins of stellar mass and far-UV luminosities respectively. Right: The De Barros et al. (2019) and predicted combined Hβ and [OIII]λ4959,5007 line luminosity function of Flares galaxies at $z \sim 8$.

Robertson B. E., et al., 2013, ApJ, 768, 71

Robertson B. E., Ellis R. S., Furlanetto S. R., Dunlop J. S., 2015, ApJ, 802, L19

Salim S., Narayanan D., 2020, arXiv e-prints, p. arXiv:2001.03181

Schaller M., Dalla Vecchia C., Schaye J., Bower R. G., Theuns T., Crain R. A., Furlong M., McCarthy I. G., 2015, MNRAS, 454, 2277

Schaye J., et al., 2015, MNRAS, 446, 521

Schwarz G., 1978, Annals of Statistics, 6, 461

Stefanon M., et al., 2019, ApJ, 883, 99

Trayford J. W., et al., 2017, MNRAS, 470, 771

Vijayan A. P., Clay S. J., Thomas P. A., Yates R. M., Wilkins S. M., Henriques B. M., 2019, MNRAS, 489, 4072

Vogelsberger M., et al., 2020, MNRAS, 492, 5167

Wilkins S. M., Bunker A. J., Lorenzoni S., Caruana J., 2011, MNRAS, 411, 23

Wilkins S. M., Feng Y., Di-Matteo T., Croft R., Stanway E. R., Bunker A., Waters D., Lovell C., 2016, MNRAS, 460, 3170

Wilkins S. M., Feng Y., Di Matteo T., Croft R., Lovell C. C., Waters D., 2017, MNRAS, 469, 2517

Yung L. Y. A., Somerville R. S., Popping G., Finkelstein S. L., Ferguson H. C., Davé R., 2019, MNRAS, 490, 2855

APPENDIX A: CALIBRATING DUST ATTENUATION

As noted in §2.3 we model the attenuation by dust on a star particle by star particle basis using the integrated line-of-sight surface density of metals as a proxy for dust attenuation. In this simple model we have a two free parameter κ_{BC} and κ_{ISM} which encapsulates the properties of dust such as the average grain size, shape, composition as well as the dust-to-metal ratio in the birth clouds and in the ISM respectively. To calibrate this model we choose an array of κ_{BC} ranging from values of 0 to 3, and then compare our UV LF to observations at $z = 5$ from Bouwens et al. (2015a) to derive a value for κ_{ISM}. The value for κ_{BC} is motivated to get better agreement with the [OIII]λ4959,5007 line luminosity and equivalent width values from De Barros et al. (2019) at $z = 8$ (see Figure A1) as well as the UV continuum slope values from literature at $z = 5$ (see Figure A2). Thus the value is a compromise between choosing a very low value of κ_{BC} that agrees with the [OIII] data while a higher value fares better for the UV continuum slope.

APPENDIX B: LUMINOSITY FUNCTION

For deriving the Schechter and double power-law fit parameters for the UVLF, we calculate the likelihood that the number of observed galaxies in a given magnitude bin is equal to that for an assumed value of the function parameters. This calculation is performed in bins of separation $\Delta M = 0.5$ mag, ranging from from our completeness limit at the faint-end to enclose all our galaxies above this limit. The bin centre and the number density of galaxies per Mag is provided in Table B1. We use the code FitDF[1] a Python module for fitting arbitrary distribution functions. FitDF uses emcee, a Python implementation of the affine-invariant ensemble sampler for Markov chain Monte Carlo (MCMC) described in Foreman-Mackey et al. (2013). The likelihood function is modelled as a Gaussian distribution (see Appendix B in Lovell et al. 2020, for the details).

We use flat uniform priors for the parameters in the functional forms. We fix narrow priors for M^* at $z = 9$ and $z = 9, 10$ for the Schechter and double power-law forms respectively. This was done since our fitting function preformed poorly in constraining the knee.

For determining which functional form is better suited at different redshifts we calculated the Bayesian Information Criterion (BIC) value for the best-fit parameters. BIC is a criterion for model selection among a finite set of models. When performing fitting it is possible to increase the likelihood by adding more parameters, but can lead to overfitting. BIC resolves this by implementing a penalty term for the number of parameters in the model; the model with a lower BIC is preferred.

APPENDIX C: OTHER EXTINCTION CURVES

There has not been any consensus across observational or theoretical studies on the exact nature of the extinction curve in galaxies, since it is closely tied to the properties of the dust grains in galaxies. And this can be inferred better by probing the galaxy SED, and studies have suggested that using a single extinction curve for every galaxy might not be right. In our study we implement a simple extinction curve that is inversely proportional to the wavelength. In
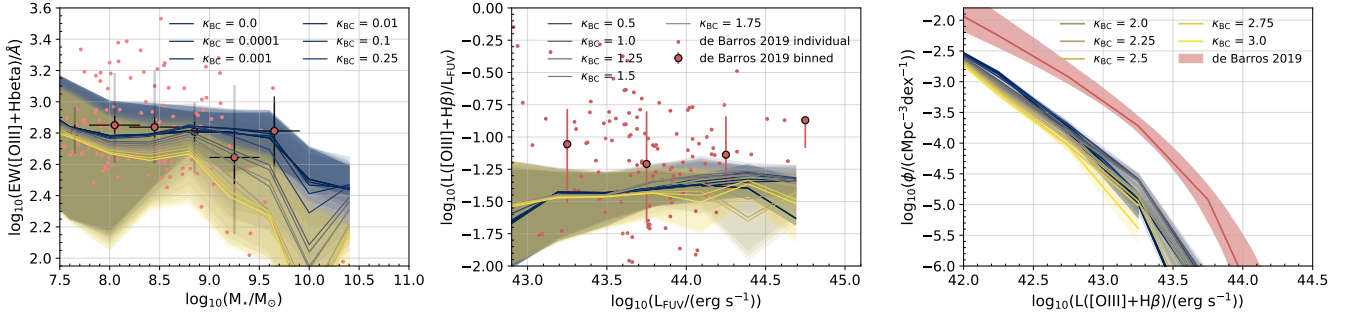
---

[1] https://github.com/christopherlovell/fitDF

Figure A1. Line luminosity and equivalent width for different values of κ_{BC}. The small red circles show the individual measurements from De Barros et al. (2019) while the large points denote the median value in bins of stellar mass and far-UV luminosities respectively.

M_{1500}	ϕ /(cMpc^{-3} Mag^{-1})	M_{1500}	ϕ /(cMpc^{-3} Mag^{-1})	M_{1500}	ϕ /(cMpc^{-3} Mag^{-1})
	$z = 5$		$z = 6$		$z = 7$
-24.245	$(3.620\pm3.620)\times10^{-8}$	-23.767	$(1.473\pm1.473)\times10^{-9}$	-23.508	$(1.473\pm1.473)\times10^{-9}$
-23.745	$(3.261\pm1.295)\times10^{-7}$	-23.267	$(3.787\pm1.329)\times10^{-7}$	-23.008	$(1.505\pm0.828)\times10^{-7}$
-23.245	$(2.218\pm1.596)\times10^{-6}$	-22.767	$(9.617\pm3.048)\times10^{-7}$	-22.508	$(9.128\pm3.036)\times10^{-7}$
-22.745	$(6.507\pm3.423)\times10^{-6}$	-22.267	$(7.815\pm2.459)\times10^{-6}$	-22.008	$4.498\pm2.214)\times10^{-6}$
-22.245	$(2.817\pm0.668)\times10^{-5}$	-21.767	$(2.692\pm0.690)\times10^{-5}$	-21.508	$(1.939\pm0.605)\times10^{-5}$
-21.745	$(6.530\pm1.155)\times10^{-5}$	-21.267	$(8.620\pm1.378)\times10^{-5}$	-21.008	$(4.658\pm1.003)\times10^{-5}$
-21.245	$(1.569\pm0.187)\times10^{-4}$	-20.767	$(1.718\pm0.204)\times10^{-4}$	-20.508	$(9.793\pm1.491)\times10^{-5}$
-20.745	$(4.672\pm0.350)\times10^{-4}$	-20.267	$(3.299\pm0.293)\times10^{-4}$	-20.008	$(2.532\pm0.257)\times10^{-4}$
-20.245	$(6.789\pm0.425)\times10^{-4}$	-19.767	$(5.165\pm0.364)\times10^{-4}$	-19.508	$(4.075\pm0.330)\times10^{-4}$
-19.745	$(9.953\pm0.527)\times10^{-4}$	-19.267	$(9.396\pm0.514)\times10^{-4}$	-19.008	$(6.639\pm0.415)\times10^{-4}$
-19.245	$(1.566\pm0.066)\times10^{-3}$	-18.767	$(1.697\pm0.070)\times10^{-3}$	-18.508	$(1.755\pm0.070)\times10^{-3}$
-18.745	$(2.571\pm0.086)\times10^{-3}$	-18.267	$(3.431\pm0.010)\times10^{-3}$	-18.008	$(3.897\pm0.107)\times10^{-3}$
-18.245	$(4.478\pm0.115)\times10^{-3}$	-17.767	$(6.178\pm0.135)\times10^{-3}$	-17.508	$(6.404\pm0.138)\times10^{-3}$
-17.745	$(7.719\pm0.152)\times10^{-3}$	-17.267	$(9.171\pm0.166)\times10^{-3}$	–	–
-17.245	$(1.105\pm0.018)\times10^{-2}$	–	–	–	–

M_{1500}	ϕ /(cMpc^{-3} Mag^{-1})	M_{1500}	ϕ /(cMpc^{-3} Mag^{-1})	M_{1500}	ϕ /(cMpc^{-3} Mag^{-1})
	$z = 8$		$z = 9$		$z = 10$
-22.682	$(2.407\pm2.407)\times10^{-8}$	-22.605	$(2.407\pm2.407)\times10^{-8}$	-22.513	$(2.407\pm2.407)\times10^{-8}$
-22.182	$(2.403\pm1.544)\times10^{-6}$	-22.105	$(2.183\pm0.872)\times10^{-7}$	-21.513	$(6.303\pm4.580)\times10^{-8}$
-21.682	$(1.451\pm0.307)\times10^{-6}$	-21.605	$(2.588\pm1.621)\times10^{-6}$	-21.013	$(9.384\pm3.790)\times10^{-7}$
-21.182	$(1.291\pm0.448)\times10^{-5}$	-21.105	$(1.291\pm0.375)\times10^{-6}$	-20.513	$(1.084\pm0.454)\times10^{-5}$
-20.682	$(4.464\pm1.026)\times10^{-5}$	-20.605	$(2.496\pm0.764)\times10^{-5}$	-20.013	$(1.242\pm0.397)\times10^{-5}$
-20.182	$(7.106\pm1.310)\times10^{-5}$	-20.105	$(4.122\pm1.009)\times10^{-5}$	-19.513	$(5.268\pm1.098)\times10^{-5}$
-19.682	$(1.429\pm0.1917)\times10^{-4}$	-19.605	$(8.132\pm1.352)\times10^{-5}$	-19.013	$(1.921\pm0.225)\times10^{-4}$
-19.182	$(3.406\pm0.301)\times10^{-4}$	-19.105	$(2.312\pm0.250)\times10^{-4}$	-18.513	$(5.412\pm0.386)\times10^{-4}$
-18.682	$(8.836\pm0.495)\times10^{-4}$	-18.605	$(7.337\pm0.451)\times10^{-4}$	-18.013	$(1.443\pm0.064)\times10^{-3}$
-18.182	$(2.201\pm0.079)\times10^{-3}$	-18.105	$(1.857\pm0.073)\times10^{-3}$	–	–
-17.682	$(3.856\pm0.105)\times10^{-3}$	-17.605	$(3.029\pm0.094)\times10^{-3}$	–	–

Table B1. Binned UVLF values.

this section we will explore how some of the observables presented before changes depending on the chosen extinction curve, namely the Calzetti (Calzetti et al. 2000), Small Magellanic Cloud (SMC, Pei 1992) and the curve used in (Narayanan et al. 2018, N18 from now on).

For this analysis we keep the value of κ_{BC} from our default model curve for these curves as well, and then use the method described in Appendix A to obtain κ_{ISM}. With that we get values of 0.018, 0.0065 and 0.02 for the Calzetti, SMC and N18 curves respectively.

This paper has been typeset from a TEX/LATEX file prepared by the author.

z	M*/Mag	$\log_{10}(\phi^*/(\text{Mpc}^{-3}\,\text{Mag}^{-1}))$	α	β	ΔBIC
5	$-21.811^{+0.040}_{-0.040}$	$-3.674^{+0.024}_{-0.025}$	$-1.987^{+0.006}_{-0.006}$	–	202.221
	$-20.998^{+0.004}_{-0.002}$	$-3.404^{+0.006}_{-0.006}$	$-1.970^{+0.006}_{-0.006}$	$-3.615^{+0.028}_{-0.029}$	
6	$-21.484^{+0.030}_{-0.028}$	$-3.868^{+0.021}_{-0.021}$	$-2.141^{+0.007}_{-0.007}$	–	12767.076
	$-20.994^{+0.010}_{-0.004}$	$-3.786^{+0.011}_{-0.010}$	$-2.204^{+0.010}_{-0.001}$	$-3.714^{+0.048}_{-0.052}$	
7	$-21.464^{+0.038}_{-0.036}$	$-4.352^{+0.031}_{-0.032}$	$-2.421^{+0.010}_{-0.010}$	–	-27.631
	$-21.692^{+0.051}_{-0.046}$	$-4.711^{+0.038}_{-0.034}$	$-2.511^{+0.009}_{-0.008}$	$-5.961^{+0.062}_{-0.029}$	
8	$-20.947^{+0.086}_{-0.085}$	$-4.379^{+0.074}_{-0.075}$	$-2.583^{+0.018}_{-0.018}$	–	18.654
	$-21.215^{+0.466}_{-0.076}$	$-4.816^{+0.397}_{-0.064}$	$-2.707^{+0.062}_{-0.015}$	$-5.659^{+1.196}_{-0.261}$	
9	$-20.806^{+0.005}_{-0.011}$	$-4.646^{+0.015}_{-0.017}$	$-2.757^{+0.012}_{-0.012}$	–	300.421
	$-21.102^{+0.001}_{-0.003}$	$-4.964^{+0.004}_{-0.005}$	$-2.750^{+0.001}_{-0.001}$	$-4.578^{+0.122}_{-0.136}$	
10	$-21.477^{+0.038}_{-0.052}$	$-6.061^{+0.027}_{-0.059}$	$-3.391^{+0.020}_{-0.052}$	–	631.045
	$-20.501^{+0.001}_{-0.002}$	$-4.727^{+0.007}_{-0.007}$	$-2.750^{+0.001}_{-0.001}$	$-5.247^{+0.103}_{-0.113}$	

Table B2. Best-fitting Schechter (first row corresponding to the redshift) and double power-law (second row corresponding to the redshift) function parameter values for the observed UVLF. In case of the Schechter fit for $z = 9$ as well as the double power-law fit for $z = 9, 10$ we implement narrow priors to M* which was set by visual inspection in order to constrain the fit. We also provide the difference of the Bayesian Information Criterion (ΔBIC) value of the best-fitting parameters of the Schechter from the double power-law function.
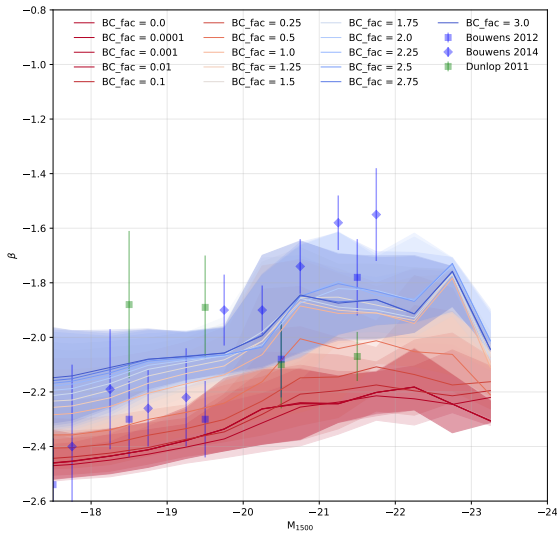

Figure A2. UV continuum slope β for different values of κ_{BC}.